A&A 491, 29–41 (2008)
DOI: 10.1051/0004-6361:20079241

Diagnostics of interstellar hydrogen in the heliosphere

Astronomy & Astrophysics
Special feature

UV optical measurements of the Nozomi spacecraft interpreted with a two-component LIC-flow model

H. Nakagawa[1], M. Bzowski[2], A. Yamazaki[3], H. Fukunishi[4], S. Watanabe[5], Y. Takahashi[1], M. Taguchi[6], I. Yoshikawa[7], K. Shiomi[8], and M. Nakamura[3]

[1] Department of Geophysics, University of Tohoku, Sendai, Japan
e-mail: `rom@stpp1.geophys.tohoku.ac.jp`
[2] Space Research Centre PAS, Bartycka 18A, 00-716 Warsaw, Poland
e-mail: `bzowski@cbk.waw.pl`
[3] Institute of Space and Astronautical Science, Japan Aerospace Exploration Agency, Sagamihara, Japan
[4] Japan Society for the Promotion of Science, Beijing, PR China
[5] Department of Earth and Planetary Science, University of Hokkaido, Japan
[6] Department of Physics, College of Science, Rikkyo University, Tokyo, Japan
[7] Department of Earth and Planetary Science, University of Tokyo, Tokyo, Japan
[8] Earth Observation Research Center, Japan Aerospace Exploration Agency, Tsukuba, Japan

Received 13 December 2007 / Accepted 8 July 2008

ABSTRACT

Aims. Following recent reports on spectroscopic observations by SWAN/SOHO suggesting that the flows of neutral interstellar helium and hydrogen in the inner heliosphere are slightly divergent, we tried to verify them on the basis of simultaneous photometric observations of heliospheric hydrogen and helium glows performed by a spacecraft located on an orbit between the Earth and Mars (which differs from the orbit of SWAN/SOHO). The observations were interpreted with the use of various independent models of interstellar hydrogen and helium in the inner heliosphere, evaluated over a mesh of parameters.

Methods. The data might suggest that the upwind and downwind directions of interstellar H may differ by less than 180°, which we interpret as due to a side shift of the secondary population of interstellar hydrogen, which might be due to a deformation of the outer heliosheath e.g. because of the action of interstellar magnetic field. The simulations we performed do not support the idea that the secondary population is significantly shifted to the side.

Results. The upwind/downwind direction of interstellar hydrogen as derived from our observations agrees within the error bars with the upwind/downwind direction of interstellar helium and the error bars include both the upwind direction of interstellar helium, derived from in-situ observations of GAS/Ulysses, and the upwind direction of interstellar hydrogen, derived from observations of SWAN/SOHO.

Key words. Sun: UV radiation – ISM: atoms – ultraviolet: ISM

1. Introduction

The Sun is located in a warm (~6500 K) and partly ionized cloud of interstellar gas. It is called the Local Interstellar Cloud (LIC), and the heliosphere surrounding the Sun is formed by interaction between the expanding solar wind and the components of the LIC (Fig. 1). The interaction region, which is referred to as the heliospheric interface, has a complex structure in which the solar wind, interstellar neutral atoms, galactic and anomalous cosmic rays, and pickup ions all play roles (Zank 1999; Izmodenov et al. 2004; Baranov 2006; Izmodenov & Baranov 2006). The interaction between the solar wind and the interstellar medium has attracted increased interest following the passage of the Voyager spacecraft through the termination shock of the solar wind (e.g. Decker et al. 2005; Stone et al. 2005). Although this achievement has spurred development of increasingly sophisticated models attempting to describe various aspects of the physics underlying the interaction between the solar wind and the interstellar medium, to our knowledge no direct observations of different components of the interstellar gas within the heliospheric interface and beyond have been reported to date. It is also difficult to understand the global structure of the heliosphere using one-point measurements. At present, the heliospheric interface structure and local interstellar parameters can only be explored by remote and indirect measurements supported by modeling.

Contrary to the interstellar low-energy charged particles, interstellar neutrals are able to penetrate deep into the heliosphere. Since neutral interstellar hydrogen is processed by interaction with local plasma during the passage through the heliospheric interface, its physical state at the nose of the termination shock is different to that in the unperturbed interstellar medium and its observation can bring insight into the processes going on within the interface. In contrast, neutral interstellar helium is only weakly coupled to the heliospheric plasma and penetrates the heliospheric interface practically without a change, so its observation yields information about the state of the unperturbed interstellar medium. A comparison of neutral hydrogen and helium populations observed from the same platform can be expected to set very tight constraints on the physical processes in the heliospheric interface region.

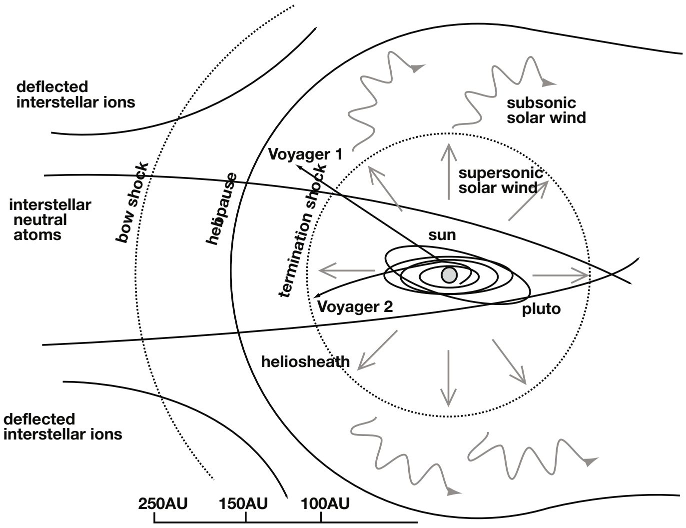

Fig. 1. Schematic drawing of the heliospheric interface, which is the boundary region between the solar wind and the Local Interstellar Cloud (LIC).

The bulk velocity, density, and inflow direction of interstellar helium were determined by an International Space Science Institute (ISSI) research team (Möbius et al. 2004) who undertook a coordinated analysis of interstellar helium data obtained simultaneously from observations of the backscattered solar ultraviolet (UV) radiation, pickup ions, and direct neutral gas diagnostics and obtained an excellent agreement between the results. Five traversals of the helium gravitational focusing cone allow us to obtain an accurate determination of the ecliptic longitude, while observations of pickup He^{++} with Ulysses give us an estimate of the absolute density 0.0151 ± 0.0015 atoms/cm^3 (Gloeckler et al. 2004). Direct neutral helium observations by the Ulysses GAS instrument indicated a flow velocity 26.3 ± 0.4 km s^{-1} from ecliptic longitude and latitude of $254.7 \pm 0.5°$ and $5.2 \pm 0.2°$ in the B1950 reference system (Witte 2004) and absolute density equal to 0.015 ± 0.003 atoms/cm^3. The flow vector was also determined by UV backscattering observations of the helium cone by the Extreme Ultraviolet Explorer (EUVE) to be 24.5 ± 2.0 km s^{-1} from ecliptic coordinates of $(254.7 \pm 0.5°, 5.7 \pm 0.5°)$ (Vallerga et al. 2004). Since these results agree very well with each other, we adopt them as our reference values and further on will refer to the final result listed by Möbius et al. (2004) as the canonical.

Interpretation of helium observations was carried out with the use of the classical hot model of neutral interstellar gas distribution in the heliosphere. This model was described, e.g., by Thomas (1978), Fahr (1978), Wu & Judge (1979), and Lallement et al. (1985). The model assumes that both the radiation pressure and ionization of the neutral gas have spherical symmetry and are constant in time, and that the distribution function of interstellar gas in a region located sufficiently far away from the Sun to be beyond the dynamical influence by the Sun is given by a Maxwellian function characterized by density, bulk velocity, and temperature. Such a model will be referred to as the classical hot model; in the past it was widely used to interpret both helium and hydrogen observations.

While in the case of helium this model was generally successful because of the lack of modifications of the gas distribution within the heliospheric interface, interpretation of neutral interstellar hydrogen observations is much more challenging. The neutral population of the interstellar hydrogen gas is modified during its passage through the heliospheric interface because of charge exchange interactions with protons. The original population of interstellar hydrogen atoms is depleted and a new neutral population is created, composed of protons neutralized through resonant charge exchange reactions. Consequently, the kinetic parameters of the newly created neutral atoms have exactly the same values as those of the parent protons just before the charge exchange reaction. Since the new atoms are not restricted by the ambient magnetic field, they can spread freely and travel large distances from their birth places without a change of their kinetic parameters, and some of them are able to penetrate the heliopause and enter the heliosphere. As a result, an additional, secondary population of neutral atoms is added to the original interstellar atomic hydrogen population at the nose of the termination shock. Its bulk velocity is lower and temperature higher than those of the primary component. The net density of neutral gas at the nose of the termination is reduced approximately by a half with respect to the density in the unperturbed medium, a phenomenon which is referred to as the filtration effect.

After penetration of the heliopause and then inside the termination shock, neutral interstellar hydrogen continues to exchange charge with the protons from the local plasma, creating additional populations of heliospheric neutral atoms. As a result, there are at least four populations:

1. the primary (original) interstellar component (assumed to be in thermal and kinematic equilibrium with interstellar protons);
2. the secondary interstellar component (from the outer heliosheath);
3. the hot heliosheath population (from the inner heliosheath;
4. the neutralized solar wind (from charge exchange between the supersonic solar wind protons and interstellar atoms inside the termination shock).

The neutralized solar wind speeds radially away from the Sun at the solar wind speed (i.e. about 400 km s^{-1}) and is Doppler-shifted away from the solar Lyman α line, which is about 150 km s^{-1} wide (Lemaire et al. 2002). Hence, the neutralized solar wind component cannot be observed by resonant backscattered emission, because the corresponding atoms cannot be excited by the solar Lyman α line. The density of the inner-heliosheath population of hot neutral atoms, resulting from neutralization of the hot (10^6 K) protons of the inner heliosheath, should be a few orders of magnitude lower than of the thermal components because of the very low values of the absolute production rate of this population. Hence the local density of the heliosheath-derived component at a distance of a few AU from the Sun should be a few orders of magnitude lower than that of the primary and secondary components. Furthermore, because of high specific velocities of individual atoms (believed to be if the order of 200 km s^{-1}) they are Doppler-shifted away from the spectral region corresponding to the thermal interstellar population. Modeling in this respect was performed by Quémerais & Izmodenov (2002), who conclude that the contribution to the wavelength-integrated signal from this component close to 1 AU from the Sun is negligible.

The primary component represents the unperturbed interstellar medium. The proton temperature in the hydrogen wall, which is the region between the bow shock and the heliopause, is about 5×10^4 K, but the secondary component of neutral gas, created in this region, after propagation to the termination shock is cooler ($\sim 2 \times 10^4$ K) (Baranov & Malama 1993, 1995; Zank et al. 1999). The velocity vector of the combined thermal populations of neutral interstellar hydrogen in the inner heliosphere can be inferred from measurements of the heliospheric Lyman α glow with the use of an H cell (Bertaux & Lallement 1984). Quémerais et al. (1999) and Lallement (2005) performed such observations using the Solar Wind Anisotropy (SWAN) instrument on board the Solar and Heliospheric Observatory (SOHO) spacecraft (Bertaux et al. 1995). Lallement et al. (2005) reported that the net flow of neutral interstellar hydrogen in the inner heliosphere (a composite of the primary and secondary components) is deflected with respect to the helium flow by about 4°. The cause of the deflection, however, remains to be discovered. Lallement et al. (2005) pointed out that the most plausible mechanism for the observed deflection is a lateral asymmetry of the heliospheric interface caused by the interstellar magnetic field. They further hypothesized that because of non-axisymmetric charge exchange between neutral hydrogen and protons of the LIC between the bow shock and the heliopause, the secondary component of neutral hydrogen will penetrate the heliosphere from a direction in the plane determined by the flow vector of the primary component and by the vector of the magnetic field in the LIC. Thus, the hydrogen and helium flow directions define the interstellar magnetic field plane. Hence the secondary component of neutral hydrogen flow may be usable as a compass sensitive to the interstellar magnetic field. If the heliosphere is distorted by an external magnetic field, the region of maximum production of the secondary component will be shifted away from the inflow axis. This behavior is connected to the deflection of the nose of the bow shock. At the same time, the nose of the termination shock should be deflected in the opposite direction, resulting in a shift of the region of maximum production of the inner-heliosheath component of hydrogen atoms. Therefore, certain imprints of the asymmetry of the heliosphere plasma interface should be observable in the distribution of neutral interstellar hydrogen flow (Izmodenov et al. 2005).

Suggestions that the interstellar gas flow could be deflected from the canonical direction or that some unexplained asymmetries are present have already been reported in the literature. Based on the analysis of a number of data sets pertaining to neutral interstellar hydrogen and helium atoms, obtained with various techniques, Collier et al. (2004) suggested an inflow of interstellar gas from an ecliptic longitude shifted by +10° ~+40° from the canonical upstream neutral interstellar flow direction of 254° (Collier et al. 2004). The reality, origin and properties of such a flow are still under debate.

Most of the previous observations of interplanetary hydrogen and helium, including measurements of pickup ions, direct measurements of neutral atoms, and measurements of heliospheric backscatter glow in the inner heliosphere, have been interpreted under the assumption that the large-scale structure of the heliosphere axially is axially symmetric (e.g. Witte 2004; Gloeckler et al. 2004; Vallerga et al. 2004). In particular, neutral hydrogen flow has been treated in a one-component approximation, although the heliosphere is filled with a mixture of collisionless components of neutral interstellar hydrogen atoms. Extrapolation into the LIC requires performing of an appropriate modeling to account for the modifications of interstellar gas by the joint action of solar gravity, radiation pressure, and ionization, and for filtering within the heliospheric interface. To our knowledge, deflection of the secondary component has not been considered until recently, and has not been investigated separately from the primary component.

The instruments on board Nozomi have proven to be of great use for heliospheric studies. Okazaki et al. (2005) reported the longitudinal variation of the heliospheric Lyman α glow and its relation to the solar photon flux, and also estimated the presence of active regions on the far side of the Sun. Nakagawa et al. (2003) investigated the distribution of the heliospheric Lyman α glow and its dependence on the phase of solar cycle based on UVS observations, and studied the solar wind mass flux and density at high latitudes of the heliosphere during the solar maximum period (Nakagawa et al., submitted). The pole-to-ecliptic flux ratio for He I was estimated based on XUV observations to be 0.61 ± 0.24 with an ionization rate of $2.3 \pm 0.27 \times 10^{7}$ s^{-1} and line width of 0.0098 ± 0.0014 nm (Yamazaki et al. 2006).

In this study, the UV imaging spectrometer (UVS) (Fukunishi et al. 1999; Taguchi et al. 2000) and extreme ultraviolet (XUV) scanner (Nakamura et al. 1999; Yoshikawa et al. 2001) observations taken by the Nozomi spacecraft were examined. The purpose of this study is to investigate whether the existence of the deflection of the inflow direction of interstellar H with respect to He reported by Lallement et al. (2005) can be verified based on photometric observations performed outside the Earth's orbit. If confirmed, we examine whether it can be explained as due to a deflection of the secondary component of interstellar neutrals relative to the main interstellar flow in the region where the interstellar medium and the heliosphere interact.

The cross-experiment observations were performed during the maximum of the 23rd solar-activity cycle, when latitudinal anisotropy in the ionization rate and related departures of the heliospheric Lyman α glow from axial symmetry are expected to be the lowest. In the following, we present an analysis of observations of both hydrogen and helium glows with the use of the hot model (Lallement et al. 1985) and we demonstrate that while it is difficult to confirm the existence of the deflection based on observations of the Lyman α glow in the upwind hemisphere, the observations of the downwind hemisphere suggest that a deflection might be present. We then discuss expected modifications of the distribution of heliospheric glow, when a deflection of the secondary component exists, and present simulations of the actual Nozomi observations of the Lyman α glow performed with the use of a state-of-the-art model, supporting two populations of the heliospheric hydrogen gas, possibly coming from different directions. Based on a comparison of these simulations with observations we realize that the presence or absence of such a deflection cannot be confirmed or rejected.

2. Observations

The Nozomi spacecraft was in a Mars transfer orbit with perihelion at 1 AU and aphelion at 1.5 AU (Fig. 2). The observations were performed during the cruise period in the Mars transfer orbit. Nozomi is a spin-stabilized spacecraft with a high gain antenna fixed on the top. It's spin axis was always directed toward the Earth. The Lyman α emission of neutral interstellar hydrogen at 121.6 nm was recorded by the UVS instrument from March 1999 until April 2002, and the backscattered emission of neutral interstellar helium at 58.4 nm was observed with the XUV instrument from 2000 until 2001. In this paper we discuss the time interval when observations in both wavebands were carried out simultaneously. The XUV scanner is mounted on one of the side-panels of the spacecraft. Its line of sight (LOS) is directed 109° anti-earthward with respect to the spin axis. The FOV is a 3.2° full-angle circular field. The spin motion of the spacecraft produces 3.2° × 360° strips in the sky. Each strip is divided into 64 sectors such that the angular resolution of each pixel is 5.625° in the spin plane and 3.2° in the plane including the spin axis. Owing to the spinning of the spacecraft and

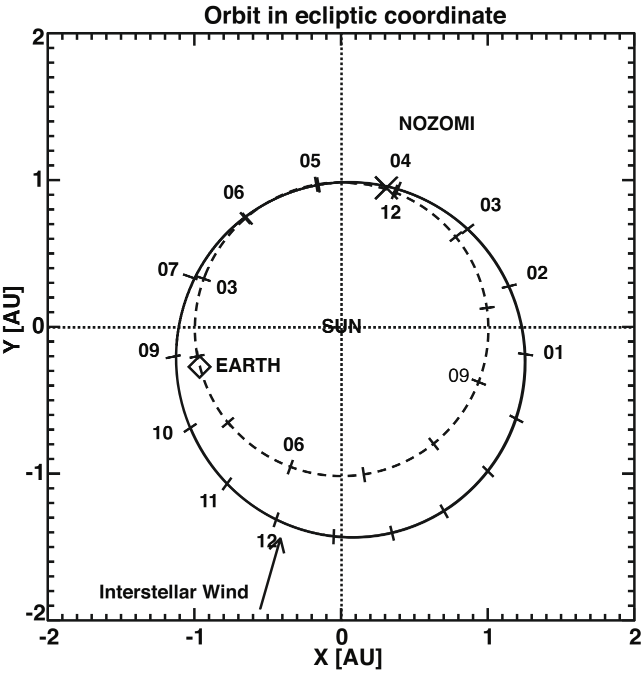

Fig. 2. Ecliptic plane projections of the orbits of Nozomi (solid line) and Earth (dashed line). The numbers at the lines represent the months during the year 2000. The cross marks the position of the spacecraft and the diamond that of the Earth on April 5, 2000, corresponding to Figs. 5, 6. The line of sight of the Lyman α observations discussed in the text are always almost perpendicular to the line connecting the Nozomi spacecraft and Earth. Note that the orbit of Nozomi is inclined at a small angle to the ecliptic plane and the lines of sight discussed in the paper are selected to pass within 5° of the ecliptic.

to the repositioning of the spin axis during the mission, the instrument covered almost the entire sky apart from small regions near the ecliptic poles. An example of the track of lines of sight during one day of observations projected on the sky along with the pointing of the spin axis and of the canonical upwind and downwind directions are shown in Fig. 4 as a broken-line oval. The data from this scan are shown in Figs. 5 and 6 shows a map of the observed distribution of the He I glow intensity. The maximum is located at DOY 90 in sector 6, which coincides with the helium focusing cone. The gray pixels represent data excluded from the analysis because of contamination by stray light and energetic particles.

The UVS instrument has two sensors: a grating spectrometer (UVS-G), operating at wavelengths between 110 nm and 310 nm with a spectral resolution of 2–3 nm, and an absorption cell photometer (UVS-P). In this study, the H Lyman α emission intensity at 121.6 nm was derived from the UVS-G data integrated over 110–130 nm. The field of view (FOV) of UVS-G is perpendicular to the spin axis of the spacecraft directed towards the Earth, allowing the UVS instrument to capture a full sky image during half of the revolution about the Sun using the spin and orbital motion of the spacecraft. The FOV in the plane perpendicular to the spin axis is equal to 0.09° and in the plane including the spin axis to 0.29°. The spin period (normally 8 s) is divided into 256 intervals for data sampling. The spatial resolution of UVS is therefore 1.41° in the plane perpendicular to the spin axis and 0.29° in the plane including the spin axis. An example track of the line of sight of UVS during one day is shown in Fig. 4 as a solid-line oval, and the observations obtained from this scan are shown in Fig. 5. One of the full-sky Lyman α intensity maps, obtained by the UVS instrument during an approximately one year interval from 17 March 2000 to 13 March 2001, is shown in Fig. 8.

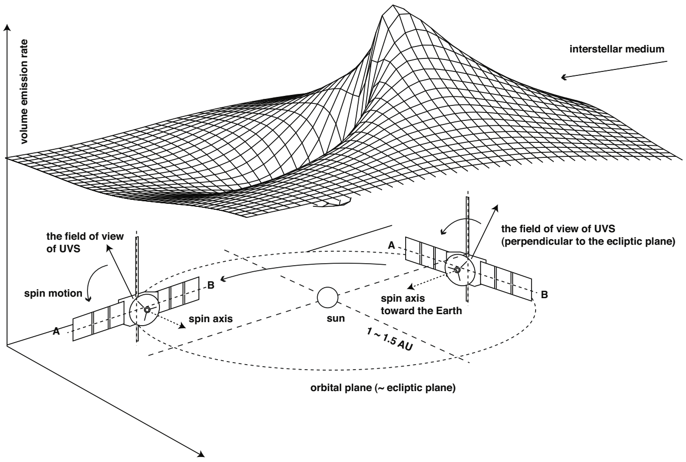

Fig. 3. Schematic representation of the geometry of Nozomi observations. The spacecraft spin axis, which coincides with the high gain antenna direction, is maintained oriented towards the Earth. The field of view of the UVS instrument is perpendicular to the spin axis of the spacecraft. Thus during each spin of the spacecraft the line of sight intersects twice the ecliptic plane, which happens at points A and B. Since the orbit of Nozomi is inclined at a small angle to the ecliptic plane, the angular separation between A and B s usually a little less than 180°. The location of the scanned strip of the sky changes in time because of the repositioning of the Nozomi rotation axis, maintained aligned at Earth, which results in changing of the longitude of points A and B. The meshed surface represents a typical distribution of the calculated volume emission rate (source function) of neutral interplanetary hydrogen, which is proportional to the local density divided by the square of solar distance.

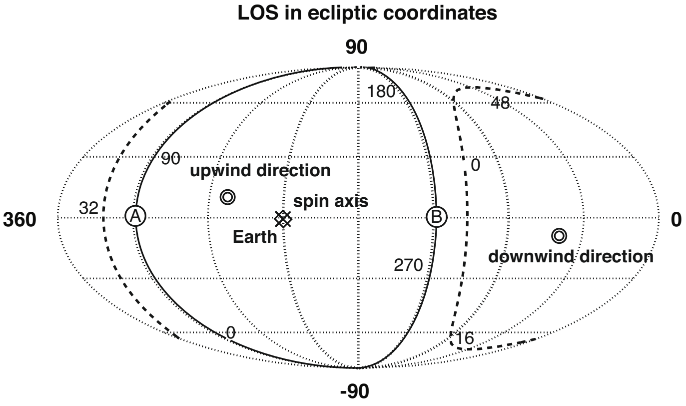

Fig. 4. Circular tracks of the lines of sight of Nozomi UVS (solid) and XUV (broken) instruments on April 5, 2000, projected on a sky map. The line of sight of XUV is inclined by 19° anti-earthward with respect to the spin plane. The directions of the spin axis and earth are shown by the cross and the diamond, respectively, and are practically identical. The canonical upwind and downwind directions are shown by the double circles. The circles A and B show the intersections of the line of sight of UVS (solid line) with the ecliptic plane. The numbers at the line of sight contour of UVS correspond to the spin angle on the horizontal axis in Fig. 5 and the numbers at the XUV contour to sector numbers on the horizontal axis in Fig. 6.

For the analysis presented in this paper, we selected data from lines of sight located within 5° of the ecliptic plane. We took this decision because this plane was intersected by the scan plane during the entire observation period, which allowed us to

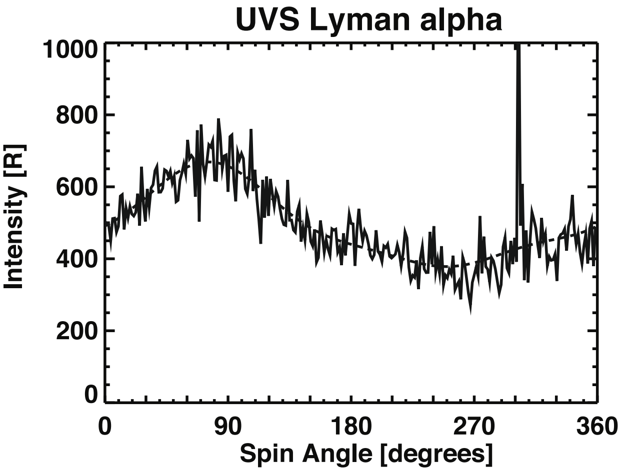

Fig. 5. The Lyman α glow intensity observed by the UVS instrument on April 5, 2000. The units of the intensity are Rayleighs. The solid line shows the original data, and the broken line the data corrected by low- and medium-pass filtering, which reduce noise and the star contamination seen, e.g., at 301°.

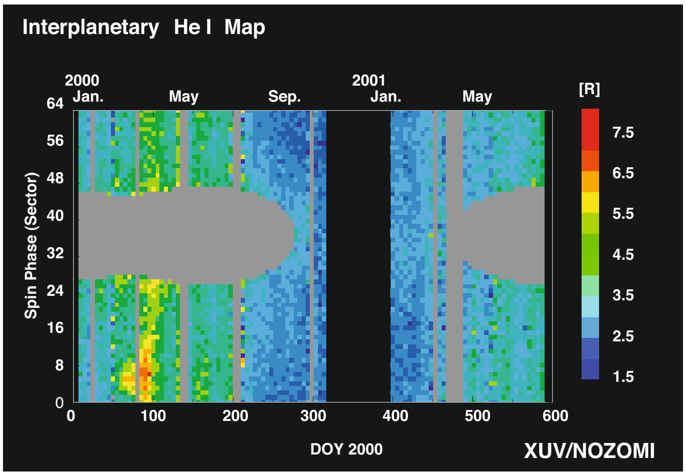

Fig. 7. Full sky intensity map of the interplanetary He 58.4 nm emission. The maximum is located at day of year (DOY) 90 and in sector 6, which is the gravitational helium focusing cone. The gray pixels show the data excluded from the analysis because of contamination by stray light and energetic particles.

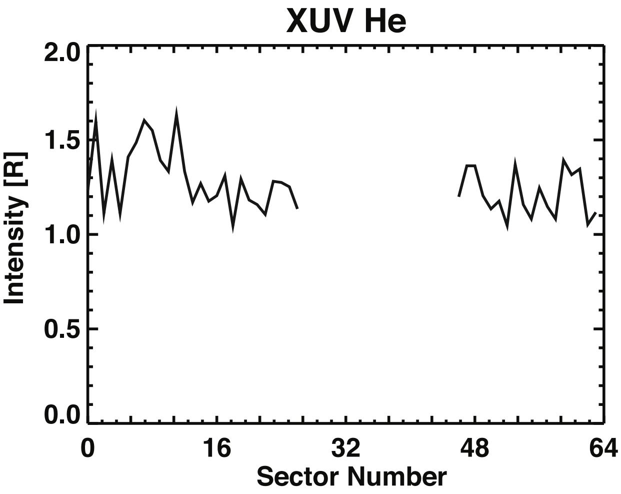

Fig. 6. The He I glow intensity observed by XUV on April 5, 2000. The units of the intensity are Rayleighs. The data around the sector number 32 are excluded from this analysis because of background due to solar stray light.

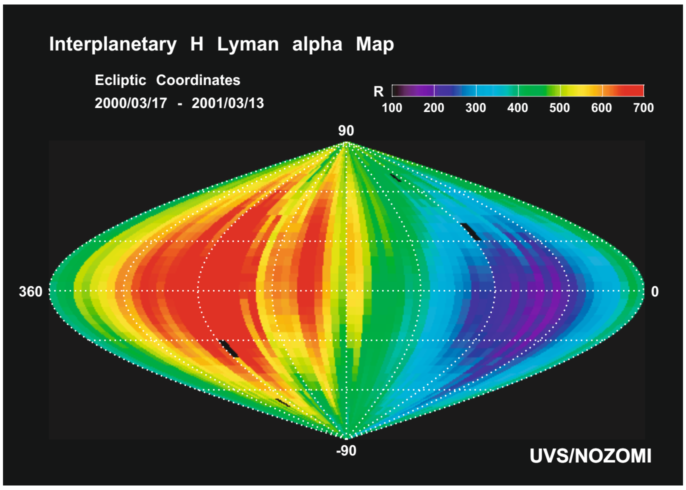

Fig. 8. Full sky intensity map of interplanetary hydrogen Lyman α emission, derived from UVS measurements performed during one year, from 17 March 2000 to 13 March 2001.

collect time series without gaps, and because this plane is the least prone to possible departures of the ionization rate and radiation pressure from spherical symmetry. At the same time, the downwind direction is close to it, so possible lateral deviations of minimum of intensity from the canonical position, determined by the downwind direction of helium, should be easily noticeable.

As shown in Fig. 4, each scan of the sky yields two intersection points with the ecliptic plane. Each repositioning of the rotation axis adds one more point to each of the two sequences of points, which below will be referred to as scan A and scan B. The points in scan A are collected from opposite directions in the heliosphere to the points from scan B. The scans can be plotted either as a function of ecliptic longitude, as in Fig. 11, or as a function of time of observation, as in Figs. 12 through 19.

3. Models

The data were interpreted using two different simulation models: one based on the hot model with one component of neutral interstellar hydrogen and a one-parameter dependence of the ionization rate on the heliographic latitude (Lallement et al. 1985), and another based on a three-dimensional and fully time-dependent model with two components of interstellar neutral hydrogen. The helium observations were interpreted using only the classical one-population hot model.

3.1. Hot model with one component of neutral hydrogen

A hot model based on the work of Lallement et al. (1985) was used to calculate the Lyman α emission intensity along the LOS of the instrument. The basic concept of the numerical simulation is described by Lallement et al. (1985). Briefly, it is assumed that the distribution function of the gas far away from the Sun (at infinity) is a Maxwell-Boltzmann function characterized by the temperature T and bulk velocity V. Radiation pressure compensates for the solar gravity to an extent depending on the intensity of solar radiation in the Lyman α line and the trajectories of hydrogen atoms are hyperbolic, with eccentricities and semi major axes determined by the ratio μ of solar radiation pressure to solar gravity. The ionization rate β_0, which is a measure of the losses in the neutral gas on its approach to the Sun, was expressed as a function of heliographic latitude b and distance from the Sun r. The ionization rate was calculated at each point along the path of a hydrogen atom during its travel through the solar system. The probability of survival of the atom until it reaches a given point in space was calculated by integrating the ionization rate probability over the entire path from infinity to the given point. The parameters of the gas at infinity were adopted as follows: bulk velocity, 20.0 km $\mathrm{s^{-1}}$; temperature, 15 000 K; hydrogen density, 0.10 $\mathrm{cm^{-3}}$. The solar radiation pressure factor μ was set to 0.99. The ionization rate of interplanetary hydrogen at 1 AU and 0° ecliptic latitude is derived from observations. The ionization rate for interplanetary hydrogen at 1 AU from the Sun is given by β_0

$$\beta_0 = \beta_{\mathrm{ce0}} + \beta_{\mathrm{ph0}} \tag{1}$$

where β_{ce0} is the charge exchange ionization rate in the ecliptic plane, and β_{ph0} is the photoionization rate. The value of β_{ce0} was calculated using the solar wind velocity and density provided by the OMNI WEB (Goddard Space Flight Center, NASA; `http://omniweb.gsfc.nasa.gov/ow.html`) after smoothing by an 81-day running mean method using the formula

$$\beta_{\mathrm{0ce}} = n\, \boldsymbol{v}\, \sigma(\boldsymbol{v}) = F \sigma(\boldsymbol{v}) \tag{2}$$

where $\boldsymbol{v}$ is the solar wind velocity, n is the solar wind density, F is the solar wind flux, and $\sigma(\boldsymbol{v})$ is the cross-section for charge exchange, which was calculated following Bzowski (2001) based on the data from Barnett et al. (1990) from the formula:

$$\sigma(\boldsymbol{v}) = 6.29 \times 10^{-15} - 7.26 \times 10^{-16} \times \ln(\boldsymbol{v})\,. \tag{3}$$

Thus, $\sigma(\boldsymbol{v})$ is a function of the relative velocity between the atoms and the solar wind protons. The photoionization rate in the ecliptic plane (β_{ph0}) was derived from measurements made with the Solar Extreme Ultraviolet Monitor (SEM) on board the SOHO spacecraft at the wavelengths from 0.1 to 50 nm (see `http://www.space.unibe.ch/soho/data.html`). The spectral profile of solar EUV radiation (0.1–91.2 nm) was calculated using the SOLAR2000 empirical model (Tobiska et al. 2000), and the cross-section for photoionization was calculated following the method of Cruddace et al. (1974). The photoionization rate in the ecliptic plane is then given by

$$\beta_{\mathrm{ph}} = \int_0^{91.2} F_\lambda\, \sigma_{\mathrm{ph}}\, \mathrm{d}\lambda \tag{4}$$

where σ_{ph} is the cross-section for photoionization, F_λ is spectral flux, and λ is wavelength. The backscatter intensities were calculated using the optically thin, single-scattering approximation with the assumption of homogeneous instantaneous illumination (i.e. spherically symmetric and corresponding to the model of radiation pressure used to calculate the densities). The parameters used in the model are summarized in Table 1.

Table 1. Values of parameters used for the classical hot model of hydrogen.

Parameters	Values
Density of hydrogen at infinity	0.10 [$\mathrm{cm^{-3}}$][1]
Velocity of hydrogen at infinity	20.0 [km $\mathrm{s^{-1}}$]
Temperature of hydrogen at infinity	15 000 [K][2]
Radiation pressure normalized by gravity for H	0.99
Ionization rate at 1 AU on ecliptic plane for H	5.0–7.0 × 10^{-7} [/s]

[1] Gloeckler (1996); [2] Costa et al. (1999).

Table 2. Boundary conditions for the three-dimensional and fully time-dependent model. These boundary conditions come from the Moscow model and were used in the Warsaw test-particle model.

Components	Density	bulk velocity	Temperature
LIC	0.18 (H), 0.06 (p), 0.015 (He)	26.4	6300
Primary hydrogen	0.03465	28.512	6020
Secondary hydrogen	0.06021	18.744	16 300

3.2. Three-dimensional, fully time-dependent model with two components of neutral hydrogen

The multi-component simulations, performed to compute the simulated UVS signal, were carried out with the use of the Warsaw kinetic test-particle model of heliospheric gas distribution (Rucinski & Bzowski 1995). The boundary conditions, ionization rates, and radiation pressure were taken from the literature. Specifically, the upwind direction of interstellar gas was adopted as determined based on Ulysses in situ observations of interstellar helium by Witte (2004) (254.68°, 5.31° in the ecliptic B1950.0 coordinates), and the bulk velocities and temperatures based on analysis of pickup ion observations and extensive Monte Carlo (MC) simulations, performed with the use of the Moscow model, reported by Izmodenov et al. (2003). The parameters of the gas in the LIC and parameters of the primary and secondary populations at the nose of the termination shock, returned by the Moscow MC model and adopted as the boundary conditions for the Warsaw test-particle model, are listed in Table 2.

The Moscow MC simulation uses an iterative gas dynamic-kinetic model of interaction between the solar wind and the local interstellar medium, and takes into account the mutual influence of the plasma component of the LIC and neutral interstellar hydrogen atoms. The interface is characterized by three surfaces: the solar wind termination shock, the heliopause, and the interstellar bow shock. The flow of interstellar gas in the heliospheric interface must be described kinetically because the mean free path of neutral atoms against collisions with each other is of the order of the size of the heliospheric interface. The kinetic distribution function in the Moscow model is obtained by solving the Boltzmann equation:

$$\begin{aligned} \boldsymbol{w}_{\mathrm{H}} \frac{\partial f_{\mathrm{H}}(\boldsymbol{r},\boldsymbol{w}_{\mathrm{H}})}{\partial \boldsymbol{r}} &+ \frac{F}{m_{\mathrm{H}}} \frac{\partial f_{\mathrm{H}}(\boldsymbol{r},\boldsymbol{w}_{\mathrm{H}})}{\partial \boldsymbol{w}_{\mathrm{H}}} = -f_{\mathrm{H}}(\boldsymbol{r},\boldsymbol{w}_{\mathrm{H}}) \\ &\times \int |\boldsymbol{w}_{\mathrm{H}} - \boldsymbol{w}_{\mathrm{p}}| \sigma_{\mathrm{ex}}^{\mathrm{hp}} f_{\mathrm{p}}\left(\boldsymbol{r},\boldsymbol{w}_{\mathrm{p}}\right) \mathrm{d}\boldsymbol{w}_{\mathrm{p}} \\ &+ f_{\mathrm{p}}(\boldsymbol{r},\boldsymbol{w}_{\mathrm{H^*}}) \int |\boldsymbol{w}_{\mathrm{H^*}} - \boldsymbol{w}_{\mathrm{H}}| \sigma_{\mathrm{ex}}^{\mathrm{hp}} f_{\mathrm{p}}(\boldsymbol{r},\boldsymbol{w}_{\mathrm{H^*}})\, \mathrm{d}\boldsymbol{w}_{\mathrm{H^*}} \\ &- \left(\beta_{\mathrm{i}} + \beta_{\mathrm{impact}}\right) f_{\mathrm{H}}(\boldsymbol{r},\boldsymbol{w}_{\mathrm{H}}) \end{aligned} \tag{5}$$

where $f_{\mathrm{H}}(\boldsymbol{r},\boldsymbol{w}_{\mathrm{H}})$ is the distribution function of hydrogen atoms, $f_{\mathrm{p}}\left(\boldsymbol{r},\boldsymbol{w}_{\mathrm{p}}\right) \boldsymbol{w}_{\mathrm{p}}$ and $\boldsymbol{w}_{\mathrm{H}}$ is the local distribution function of protons (assumed to be Maxwellian), $\boldsymbol{w}_{\mathrm{p}}$ and $\boldsymbol{w}_{\mathrm{H}}$ are the individual proton and hydrogen atom velocities, $\sigma_{\mathrm{ex}}^{\mathrm{hp}}$ is the cross-section of charge-exchange between a hydrogen atom and a proton, β_{i} is the photoionization rate, m_{H} is the mass of a hydrogen atom, β_{impact} is the electron impact ionization rate, and F is the vector sum of the gravitational force and solar radiation pressure force. This equation takes into account the effects of resonance charge-exchange, photoionization, and electron-impact ionization, as well as solar gravitation and solar radiation pressure. After running a pure gas-dynamical model of the heliosphere without neutrals, a two-shock, pure-plasma solution with the termination shock, heliopause, and bow shock is obtained. Then, taking the plasma conditions throughout the heliosphere from the results of this calculation, an MC simulation is carried out to derive the distribution of neutral interstellar hydrogen gas. After the first-step solution for the hydrogen distribution is obtained, feedback due to the effect of neutral hydrogen on the heliospheric plasma is calculated, a corrected plasma distribution is computed and the MC simulation is iterated until the neutral gas and plasma solutions converge and stop changing from one iteration to another.

The baseline Moscow MC model is axially symmetric and static. A recently developed time-dependent model (Izmodenov et al. 2005; Izmodenov et al. 2008) requires extremely powerful computers to run and still lacks a description of latitudinal anisotropy in the ionization rates. Nevertheless, a model able to reproduce these effects inside the termination shock is needed. This model is the Warsaw test-particle model, which was run with the boundary conditions shown in Table 2. The first description of the computational method used was presented by Rucinski & Bzowski (1995), where the expected amplitudes of density modulation and backscatter intensity are also reported for an axially symmetric approximation. In order to obtain the density and bulk velocity of interstellar gas for a given moment in time and location in space R, we must calculate the local distribution function $f\left(x, y, z, v_{\mathrm{x}}, v_{\mathrm{y}}, v_{\mathrm{z}}, \tau\right)$ and integrate in the local velocity space. To that end, the position and velocity vector of the atom and its survival probability are tracked numerically backwards in time based on the following set of equations in the local Cartesian coordinates:

$$\frac{\mathrm{d}}{\mathrm{d}t}\begin{bmatrix} x \\ y \\ z \\ v_x \\ v_y \\ v_z \\ u_v \end{bmatrix} = \begin{bmatrix} v_x \\ v_y \\ v_z \\ -\frac{GM(1-\mu(t))}{r(t)^{-3}}x \\ -\frac{GM(1-\mu(t))}{r(t)^{-3}}y \\ -\frac{GM(1-\mu(t))}{r(t)^{-3}}z \\ -\frac{\beta(t)r_e^2 u_v}{r_t^2} \end{bmatrix} \tag{6}$$

where G is the gravitational constant, M is the mass of the Sun, t is time, $r = \sqrt{x^2 + y^2 + z^2}$, u_{v} is the probability of survival against ionization of the relevant atom in its orbit, and $\mu(t)$ and $\beta(t)$ are the time-dependent normalized radiation pressure and ionization rate at $r_{\mathrm{e}} = 1$ AU. The atom is traced back to the termination shock, which is so far from the Sun that the effects of the solar dynamical influence can be neglected. The back-tracking procedure returns the values of the velocity vector of the atom at the termination shock $V_{\mathrm{TS}} = \left(v_{x,\mathrm{TS}}, v_{y,\mathrm{TS}}, v_{z,\mathrm{TS}}\right)$ and its survival probability. With these in hand, we can calculate the kinematic weight of the atom $\omega_{\max,w}$ (i.e., the probability that such a test atom exists at the termination shock), and its ionization weight ω_{ion}, (which is equivalent to the probability that the atom survives its travel from the termination shock to the local point), which is calculated using the following standard formula:

$$\omega_{\mathrm{ion}}(\tau) = \exp\left(-\int_{\infty}^{\tau} \beta(t)\left(r_{\mathrm{e}}/r(t)\right)^2 \mathrm{d}t\right) \tag{7}$$

where $r^2(t) = \sqrt{x^2(t) + y^2(t) + z^2(t)}$ and r_{e} is a reference distance, usually adopted as equal to 1 AU. A product of these two probabilities allows us then to define the local distribution function as:

$$\begin{aligned} f\left(x, y, z, v_x, v_y, v_z, \tau\right) &= \omega_{\max,x}\left(x_{\mathrm{TS}}, y_{\mathrm{TS}}, z_{\mathrm{TS}}, v_{x,\mathrm{TS}}, v_{y,\mathrm{TS}}, v_{z,\mathrm{TS}}\right) \\ &\times \omega_{\mathrm{ion}}\left(x, y, z, v_x, v_y, v_z, \tau\right). \end{aligned} \tag{8}$$

The numerical integration of orbits and survival probabilities is carried out with the use of the efficient recurrent power series (RPS) method, as adapted from Sitarski (1979) and discussed in the appendix of Rucinski & Bzowski (1995). Numerical integration of the local distribution function over the local velocity space returns the hydrogen density at the spatial point $R = (x, y, z)$ for each epoch τ:

$$n(x, y, z, \tau) = \int_0^{2\pi} \mathrm{d}\lambda \int_{-\pi/2}^{\pi/2} \cos\phi \mathrm{d}\phi \int_0^{\infty} v^2 \mathrm{d}v f(x, y, z, v, \lambda, \phi, \tau) \tag{9}$$

where the integration is performed in the velocity space in the spherical coordinates related to the Cartesian coordinates in the following way:

$$v_x = v \cos\lambda \cos\phi \tag{10}$$

$$v_y = v \sin\lambda \cos\phi \tag{11}$$

$$v_z = v \sin\phi \tag{12}$$

$$v^2 = v_x^2 + v_y^2 + v_z^2. \tag{13}$$

In the two-population approach, this computation scheme is applied twice for two different sets of parameters for the gas at the termination shock. One set of the parameters corresponds to the primary population returned by the Moscow MC model, the other one to the secondary population, with, additionally, the upwind direction varied on a mesh presented elsewhere in the paper. The results of these calculations are co-added, thus yielding the local density of neutral interstellar hydrogen in the inner heliosphere.

Iterating this procedure for appropriately selected space points and time moments yields the relevant hydrogen density distribution, allowing the evolution to be monitored over the solar cycle. The most important feature of this calculation is that both the ionization rates and radiation pressure are based on actual observations. Figure 9 shows monthly averages of radiation pressure expressed in the units of solar gravity, computed for each moment of the Nozomi observations. These monthly averages are used to compute the simulated intensities corrected for fluctuations of the solar illumination. The model is fitted to the Lyman α time series obtained from SOLAR2000 v 1.24 (Tobiska et al. 2000; Bzowski 2001). For simplification, the solar line profile was assumed to be flat, so that the radiation pressure does not depend on the radial velocity of the atoms. In reality, the solar line profile is not flat, corresponding to a ca. 10% change in neutral hydrogen density.

A scaling coefficient for the line center/line integrated ratio was applied, as obtained by Bzowski et al. (2008). The solar full-disk Lyman α profiles were obtained from Lemaire et al. (2002) and are shown in Fig. 10. The ionization processes are simulated as a sum of the charge-exchange of H atoms with solar wind protons, photoionization, and electron impact, as summarized by Bzowski et al. (2008). Daily charge-exchange rates are computed from daily in-situ observation parameters, compiled in the OMNI-2 data (OMNI WEB, Goddard Space Flight Center,

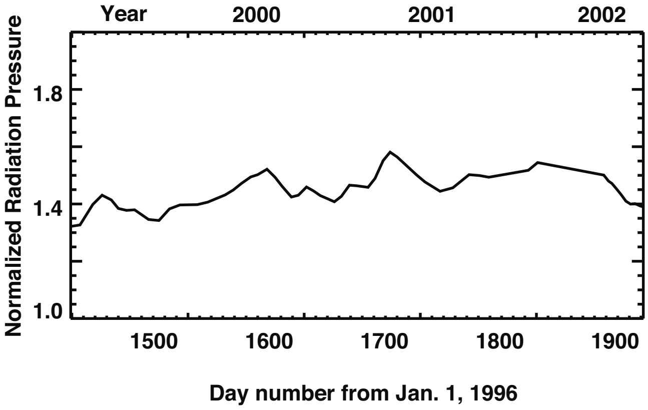

Fig. 9. Time variations of the ratio of solar radiation pressure to solar gravity, used in the three-dimensional fully time-dependent hydrogen model. Monthly averages are computed for each moment of the Nozomi observations from a time series of the solar Lyman α flux returned by the SOLAR2000 model.

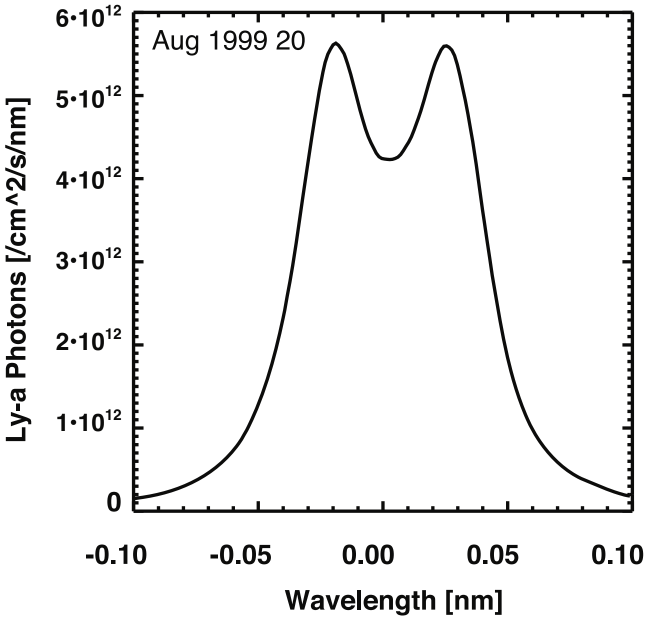

Fig. 10. The solar Lyman α line profile for a date corresponding to the Nozomi observation, taken from Lemaire et al. (2002).

NASA). The rate of ionization by charge-exchange is proportional to the local flux of the solar wind and to the cross section for charge exchange. The cross-section depends on the relative velocity between the colliding particles. Since, from conservation laws, the solar wind flux depends on the solar distance as $1/r^2$, then, based on Eq. (2),

$$\beta_{\text{ce}0}(t) = \sigma_{\text{ce}}(v)\, n(t)\, v(t)/r^2 \tag{14}$$

$$\begin{aligned}\sigma_{\text{ce}}(v) &= -2.01848 + 1.00136 \times 10^{-15} \ln^2 v \\ &\quad - 1.71725 \times 10^{-14} \ln v + 1.03807 \times 10^{-13}\end{aligned} \tag{15}$$

where v is the solar wind speed at time t. The latitudinal dependence of the charge-exchange ionization rate was estimated from SWAN optical observations of the interplanetary Lyman α emission (Bzowski et al. 2003) and approximately by the following formula (Bzowski et al. 2008):

$$\beta_{\text{ce}}(\phi, t) = (A + B\phi) + (\beta_0(t) - A) \exp\left[-\frac{\ln 2\,(2\phi - \phi_{\text{N}} - \phi_{\text{S}})^n}{(\phi_{\text{N}} - \phi_{\text{S}})^n}\right] \tag{16}$$

where ϕ is the heliographic latitude, ϕ_{N} and ϕ_{S} are the north and south boundaries of the equatorial band of enhanced ionization rate (the ionization bulge), defined as the north- and south-half width at half maximum, A and B are parameters of the north-south asymmetry function, derived from the 1995 Ulysses fast latitude scan (A is the mean ionization rate at the poles at the epoch of the Ulysses fast scan in 1995, B is the slope of the linear function). The photoionization rate is computed from the 10.7 cm radio flux proxy by the following conversion formula (Bzowski 2001):

$$\beta_{\text{ph}} = 8.766 \times 10^{12} F_{10.7}\left[\text{W/m}^2\right] - 5.84576 \times 10^{-10} \tag{17}$$

where $F_{10.7}$ is the 10.7 cm radio flux. This EUV ionization rate depends on the heliocentric distance according to $1/r^2$. The electron impact process is less important, with non-vanishing consequences only to ~2 AU from the Sun. The electron impact ionization rate used in the simulations is a simplified formula proposed by Bzowski et al. (2008), based on averaged solar wind electron parameters.

It is assumed that all the variations of the factors affecting the ionization rate propagate instantaneously. While such an assumption is fully justified in the case of photoionization, it is not fully accurate in the case of the charge-exchange process (it takes approximately 1 year for a disturbance in the solar wind to propagate from 1 AU to the termination shock). Since, however, the maximum of the backscattered Lyman α signal comes from about 3–5 AU from the Sun and since most of the ionization losses of neutral interstellar hydrogen occur inside ~10 AU from the Sun, where the solar wind propagation time does not exceed ~1.5 months, the assumption of instantaneous propagation does not introduce serious discrepancies. The distribution function of each of the two components is assumed to be Maxwellian, with parameters constant along the termination shock. With the parameters as stated above, the hydrogen density model is three dimensional and fully time-dependent. The backscatter intensities are calculated using an optically thin, single-scattering approximation, which means neglecting multiple scattering of the Lyman α photons on the heliospheric gas atoms (Quémerais 2000). The solar illuminating flux is by no means spherically symmetric and it fluctuates on time scales comparable to the solar rotation period. Hence, the non-radial LOS of Nozomi/UVS cannot be assumed to be illuminated by a spherically symmetric flux. The scale of the fluctuations can be observed in the SOLAR2000 time series, which was used to derive the normalized radiation pressure as shown in Fig. 9. In the simulations presented further on in the paper it was assumed that the solar illumination is spherically symmetric (hence the whole line of sight is illuminated by the same solar flux) and its values correspond to the SOLAR 2000 values relevant for a given date, and averaged over one solar rotation period.

3.3. Neutral helium flow

To interpret the observations of the heliospheric helium glow, the classical hot model based on Wu & Judge (1979) was used. The model is static and does not support electron ionization. The only free parameter in these simulations was the downwind direction. It was varied about the canonical downwind direction as determined by Witte (2004) from 20° to +10° in ecliptic latitude and from 65° to 95° ecliptic longitude in 5° steps. Other parameters in the computation are summarized in Table 3.

Table 3. Values of parameters used for the classical hot model of helium.

Parameters	Values
Density of helium at infinity	0.015 [cm^{-3}][1]
Velocity of helium at infinity	26.4 [km s^{-1}][2]
Temperature of helium at infinity	6300 [K][1]
Radiation pressure normalized by gravity for He	0.0
Ionization rate at 1 AU on ecliptic plane for He	2.25×10^{-7} [/s][3]

[1] Witte (2004); [2] Witte (2004); Vallerga et al. (2004); Gloeckler et al. (2004); [3] Yamazaki et al. (2006).

4. Results

4.1. Variation of emission intensity in the ecliptic plane

Figure 11 shows scans A and B of the observed emission intensities of the heliospheric Lyman α glow, normalized to their respective mean values. The two series of intensities are plotted as a function of the ecliptic longitude λ of the LOS. The fluctuations in the Lyman α emission intensity are the sources of the searchlight effect due to enhancements of the disk-integrated solar Lyman α flux by solar activity regions (Bertaux et al. 2000; Quémerais & Bertaux 2002; Okazaki et al. 2005).

The intensities for a given longitude in the two scans were observed from different locations at the Nozomi orbit and hence should present a parallax effect. This effect is a shifting of the region of maximum intensity of the heliospheric glow with respect to fixed stars, depending on the ecliptic longitude of the observer. It is related to the structure of the source function of the heliospheric glow, whose maximum (i.e., the region of maximum contribution to the net signal) is located at 3 to 5 AU at the upwind side. This region is observed from different locations along the orbit and thus is projected onto different portions of the sky. We do see this effect in our observations. The data shown in Fig. 11 were fitted with a sine function. The maximum values of the model functions, which indicate the region of maximum intensity from each locations, occur at $\lambda = 250.532°$ and 256.469° for the two lines. Their arithmetic average is equal to 253.5°, which is very close to the canonical upwind direction value of ~254°. Even though the geometry of observations and its line of sight were not perfectly symmetric with respect to the upwind direction, the simulations we performed indicated that the parallax effect for Nozomi was nearly symmetric with respect to the upwind longitude, and thus the average value of the longitudes of emission maximum is a good approximation for the upwind direction.

To investigate the cause of these discrepancies, a parameter study was conducted to estimate the effects of variations in velocity (V), temperature (T), ionization rate (β_0), anisotropy of ionization rate (A_c), and normalized radiation pressure (μ). The parameter mesh was the following: velocity ($V = 15, 20, 25$ km s^{-1}), temperature (T = 8000, 11 000, 13 000, 15 000 K), ionization rate (β_0 = 4.0, 5.0, 5.9, 7.1, 8.3, 10.0 × 10^{-7} s^{-1}), anisotropy of the ionization rate (A_c = −0.67, −0.21, 0.0, 0.007, 0.042, 0.147, 0.31, 0.40). No combination of these parameters of interplanetary hydrogen appears to explain such a significant discrepancy; in particular no combination of parameters of the model resulted in elimination of the phase shift of the simulation lines with respect to the data. Additional effects are therefore needed to provide a satisfactory explanation.

We thus performed simulations using the one-component model with the upwind directions of the hydrogen inflow of 234° (i.e. –20° from the canonical upwind direction) and 274° (+20°). The latitude was unchanged at 7°, as in the previous case. The results are shown in Fig. 13. It appears that scan A is better fitted with an upwind longitude of 274°, while scan B is better fitted with 234°, but still no combination of parameters allows a fit of both scans A and B simultaneously.

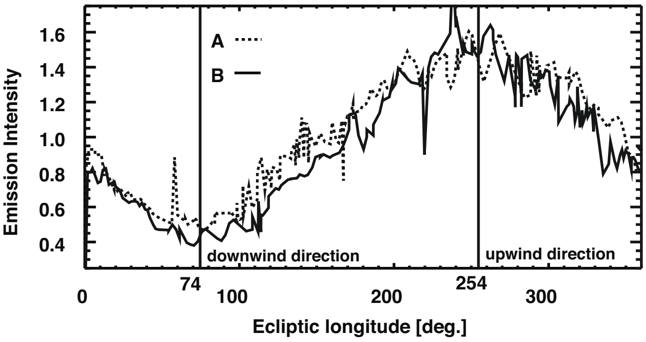

Fig. 11. Intensity of the Lyman α backscatter emission observed by UVS on scans A and B, normalized to their respective mean values and shown as a function of the ecliptic longitude. The scanning in the longitude was performed by repositioning the spin axis of the spacecraft towards earth; thus each point on a scan line was observed on a different date and from a different location in the heliosphere. The canonical upwind and downwind directions are shown by the vertical bars.

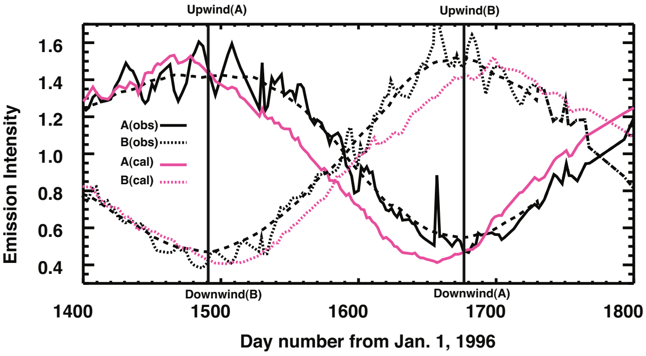

Fig. 12. Simulated intensities of the Lyman α backscatter emission, calculated for the Nozomi in-ecliptic observations with the use of the one-population hot model (pink lines), normalized to the respective mean values, compared with the observations (black lines) shown in Fig. 11. The horizontal axis is the day number from January 1, 1996. The upwind direction in the calculations was set to the canonical direction (254°). The solid lines correspond to scan A, and the dotted lines to scan B. The broken lines represent the 27 day running averages of these observations. The vertical bars show the days when the lines of sight are supposed to pass through the longitude of the canonical upwind and downwind directions.

4.2. Comparison with the two-component model

As shown above, a static model cannot fully explain the observation results with conventional parameters when a single population of interstellar hydrogen is allowed for. We thus tried an approach that on one hand would take into account the upwind direction of the interstellar gas according to helium observations, and on the other hand would make it possible to explain the phase shift particularly clearly visible in the downwind region. We used the two-population approach discussed in Sect. 3, with the upwind direction of the secondary population treated as a free parameter. The model consistently takes into account the time variations in the radiation pressure and the time- and latitude variations in the ionization rate, and we made sure we

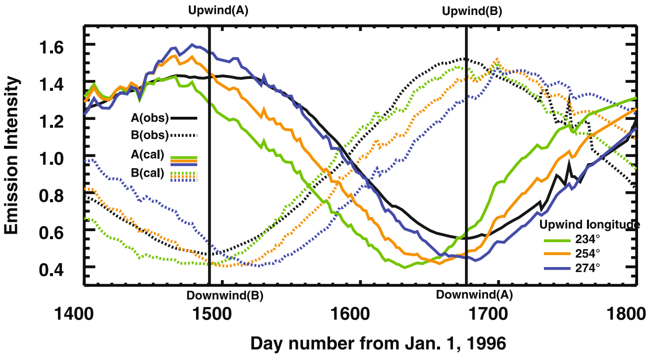

Fig. 13. Variations of simulated intensity of the heliospheric Lyman α emission for scans A and B, calculated with the use of the one-population hot model for three different upwind directions of interstellar gas: canonical 254°(*orange*), 274°(*blue*), and 234°(*green*). The black lines are the smoothed observations curves, identical to the black broken lines in Fig. 12. The vertical bars mark the upwind and downwind directions.

use up-to-date models of these parameters, based on observations.

Simulations with the one population model showed that for the geometry of Nozomi observations the minima and maxima of the observed intensity sequences are in anti-phase, which is in disagreement with the actual observations. Following the two-population approach, we enabled differentiation of the relative positions of the minima and maxima of the simulated intensities as a function of the observation time or of the longitude of the line of sight.

Simulations were performed using the two-population model with both populations coming from the same direction and with the remaining parameters taken as discussed above. Consequently, it was shown that the contribution of the secondary population to the net signal of the backscatter glow for the observations geometry of Nozomi is between 55 and 60% for the LOS directed towards the upwind hemisphere, and it systematically increases with increasing offset angle from the upwind direction, reaching about 80% for the downwind direction. This effect is illustrated in Fig. 14. It can be explained by the fact that the secondary population is significantly warmer than the primary population and hence a larger percentage of its atoms are relatively fast – a paradox, given its bulk velocity at the termination shock equal to about 65% of the velocity of the primary population. The faster atoms are less readily eliminated by ionization than the atoms from the cool primary population. The primary population has a relatively low thermal spread and thus its atoms become ionized more homogeneously as a function of their location in the velocity space. Consequently, in the downwind region mostly the secondary population survives. Then, if its upwind direction differs from the upwind direction of the primary population, we should see a shift of the minimum of intensity to the opposite side with respect to the direction of the upwind shift. Some effect in the intensity should also be visible in the upwind hemisphere, but since the maximum is broader in longitude than the minimum, and since in the upwind hemisphere the relative contribution of the secondary population to the net signal is lower than in the downwind hemisphere, the side shift effect of the maximum should be less pronounced than in the downwind direction.

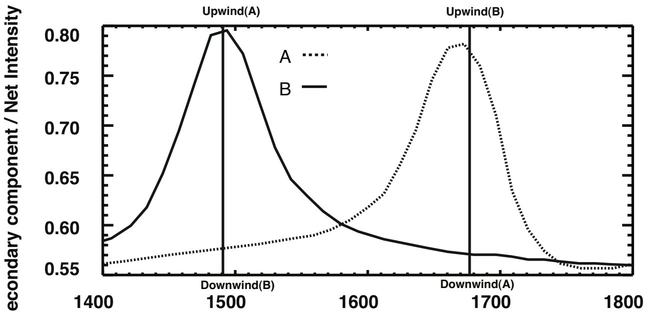

Fig. 14. The ratio of the glow intensity from the secondary component to the net intensity along the two sets of Nozomi lines of sight (A and B) in the ecliptic plane. The vertical bars mark the upwind and downwind positions.

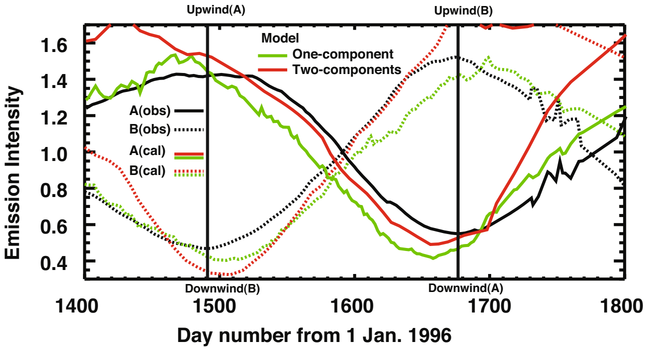

Fig. 15. Comparison between the Lyman α intensity observed by UVS and calculated in the simulations. The black lines show the variation of the Lyman α intensity observed by UVS at scans A (solid) and B (dotted) in the ecliptic plane (±5°). The green lines show the calculated intensity derived from the two-component model. Each result is plotted as an intensity normalized to its mean value over the time span. The vertical bars mark then upwind and downwind positions.

This portion of the simulations was carried out for one day each week over 56 weeks during the Nozomi observations. The upwind direction of the secondary component was varied with 3 steps of 20°, straddling the canonical 254° longitude, and with the upwind latitude of the secondary component set at 1.1°, 5.6°, 8.5°, 11.7°, and 14.9°, with the ecliptic longitude set at 254.68°, and the upwind direction of the primary component kept unchanged. The models with one and two components inflowing from the same direction are compared in Fig. 15. The two-component model helps to reduce the discrepancies noticed between the observations and the one-component computations, although the result tends to be overestimated after day 1700 and prior to day 1450.

Results of the simulations with the upwind direction of the secondary population offset from the canonical direction are shown in Figs. 16 and 17 with an expanded scale around the two minima. A residual analysis for this period is shown in Fig. 18. It shows that somewhat better agreement is obtained when the upwind direction of the secondary population is shifted by ±20° from the ecliptic longitude 254°, while the upwind direction of the primary component remains unchanged. At the minimum near day 1500, a better agreement is obtained with the upwind direction of 234°, while 274° provides a better result at the second minimum near day 1670. While the simulated intensities fit well on one side of the minimum, they diverge from the observations substantially on the other side. Inspection of Fig. 18 shows that still larger shifts would be needed to better match the

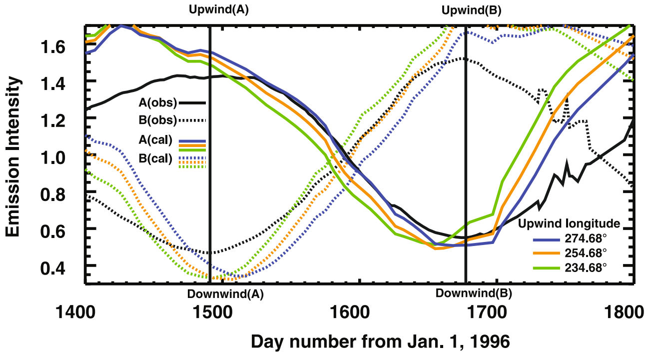

Fig. 16. Comparison between Lyman α intensity observed Nozomi/UVS and calculated using the two-component models. The black lines show the variation of the Lyman α intensity observed by UVS on two lines of sight, A (solid) and B (dotted), located within ±5° from the ecliptic plane. The green, orange, and blue lines show the calculated intensity for which the upwind longitudes of the secondary component of heliospheric hydrogen are given as 234.68°, 254.68°, and 274.68°. The latitude is unchanged. The vertical bars mark the upwind and downwind positions.

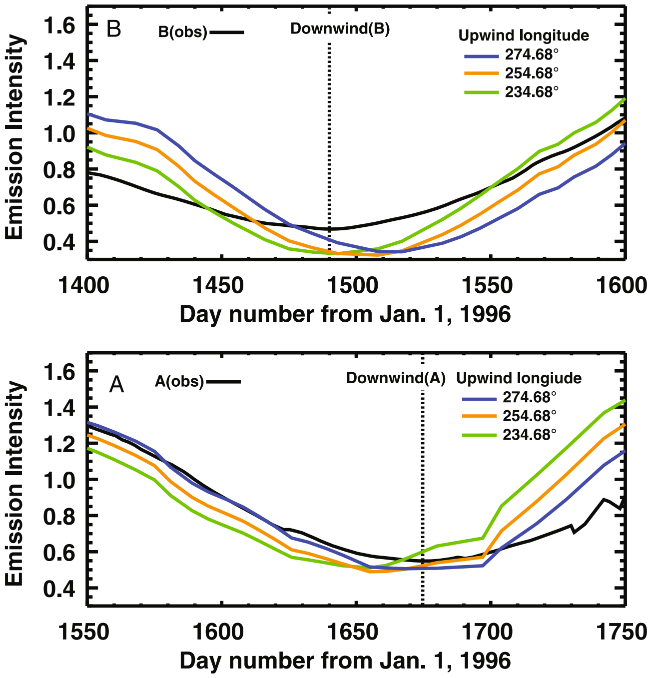

Fig. 17. Expanded views of the area in the downwind direction for scans A and B. The format is the same as in Fig. 16.

observations, but the directions of the shifts for scans A and B should be opposite.

Changing the upwind latitude of the secondary component with longitude unchanged has little effect on the results. An illustration is shown in Fig. 19. It should be noted, however, that the geometry of the Nozomi observations renders the data largely insensitive to differences in latitude. Based on these results we conclude that the discrepancies are not caused by inappropriate treatment of various populations of neutral hydrogen in the inner heliosphere.

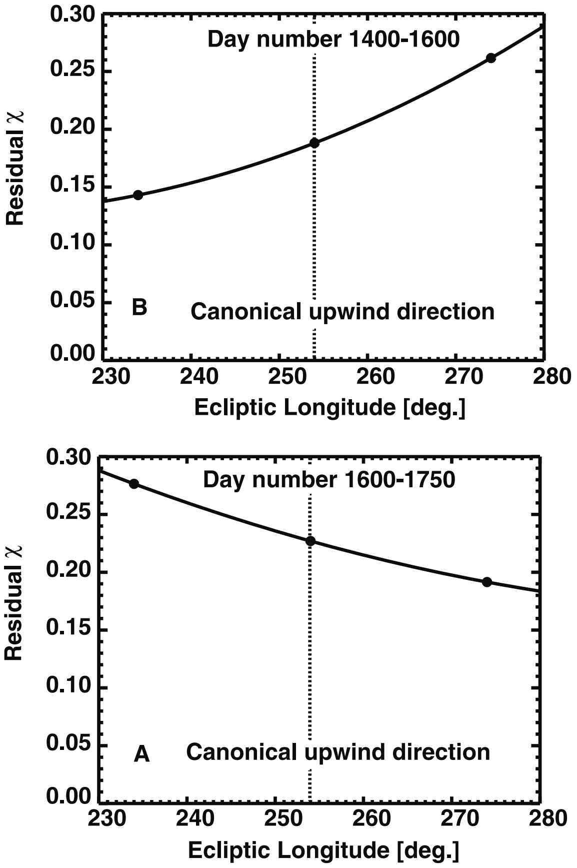

Fig. 18. Diagnostics by residual χ^2 for the scans A and B in the downwind direction, seen in Fig. 17.

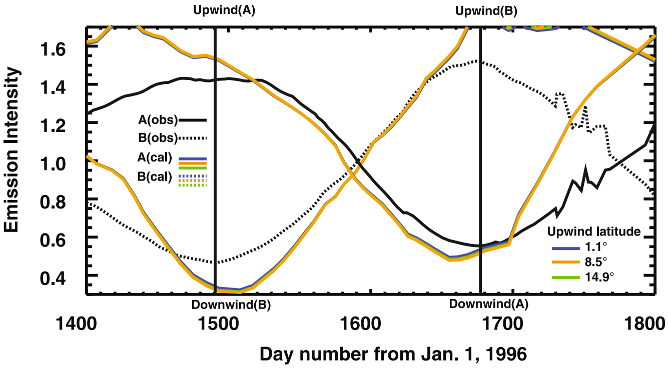

Fig. 19. Comparison between the observations and calculations performed with the use of the two-component model. The upwind directions for the secondary component were set to 1.1°, 5.6°, 8.5°, 11.7°, and 14.9° in the ecliptic latitude and 254.68° in the ecliptic longitude. The red and purple lines show the UVS data, while the yellow, green, and blue lines show the results performed for 1.1°, 8.5°, 14.9°, respectively. The vertical bars mark the canonical upwind and downwind positions.

4.3. Neutral helium flow

Residuals of simulated intensities with respect to observations attained minimum values for a downwind direction of (78.78°, –3.48°), corresponding to an upwind direction of (258.78°, 3.48°). These values are in agreement, within error bars, with the downwind direction inferred by Witte (2004) and with the upwind direction determined by Lallement et al. (2005).

5. Discussion

The full-sky fit for the upwind direction of interstellar helium is in very close agreement with the results obtained from previous studies (254.4 ± 0.5°, 5.2 ± 0.2°) (Witte 2004; Vallerga et al. 2004; Gloeckler et al. 2004). Geometrical analysis of the scans of the Lyman α glow suggests an agreement, within much larger error bars, both with the helium direction and with the hydrogen direction inferred by Lallement et al. (2005). In fact, Fig. 16 shows that the two-component model simulations for the observation set A overestimate the emission intensity before day 1450 and on the contrary underestimate it after day 1700. The opposite situation occurs for the observation set B. The observed and simulated scans show systematic differences which could not be eliminated either by variation of the gas parameters at the termination shock, or by separate treatment of the two thermal populations of interstellar gas, with possible variation of the upwind direction of one of them.

This may suggest that effects other than a shift of the secondary component could be responsible for the deviations, such as an asymmetric solar illumination and extraheliospheric background. Such effects are difficult to account for because of insufficient data from solar observations. The cause of the asymmetric behavior of the intensity in the downwind region is still debatable. Nevertheless, as demonstrated in this study, a better agreement between observations and simulations can be achieved by considering two components instead of one. This fact supports the validity of the kinetic approach used in the simulations. To explain the discrepancies between the data and the model that were found in this study, further improvements of the model should be made, for instance the distribution function of interstellar gas at the termination shock in reality is not bi-Maxwellian (Izmodenov 2001). Even when the bi-Maxwellian approximation is adopted, the parameters of the approximation function should vary as a function of the offset angle from the upwind direction. A more accurate modeling of the variations and fluctuations of the solar Lyman α flux and of the ionization rate is also an urgent need.

Bzowski et al. (2008) showed an example of differences between a superposition of two classical hot models (with the parameters corresponding to the primary and secondary populations of interstellar gas) and of the Moscow MC model evaluated for identical parameters of the gas and identical radiation pressure and ionization rates along the crosswind line between ~1 and ~5 AU from the Sun, i.e. in the region that strongly contributes to the backscatter signal. The hot model systematically overestimates the density and the discrepancies increase with the decrease of solar distance; the differences are a function of the offset angle from the upwind direction. The cause is the fact that the hot model assumes that the boundary conditions at the termination shock are homogeneous, which is not true: all the parameters of the distribution function change along the shock and the density of the gas decreases with the increasing offset angle from upwind. Thus most heavily affected are the downwind regions.

Another deficiency in our approach is the model of intensity of backscatter glow. We adopted the simplest single-scattering, optically thin model, while Quémerais (2000) showed that a more sophisticated, multi-scattering model of radiation transport in the heliosphere is needed, which, however, is very demanding computationally. The largest differences between the results of such a model and the results of the single-scattering, optically thin model adopted in this paper are noted for the lines of sight that do not go radially away from the Sun, especially in the downwind region.

One more deficiency is apparently an insufficient accuracy of the time dependent models of the radiation pressure and ionization rate. We adopted highly smoothed models, including periodicities on time scales of ~3 years and longer. Apparently, much finer scales are needed to correctly render details in the local gas density distributions, especially during solar maximum, when our observations were performed.

6. Conclusions

Simultaneous photometric observations of the heliospheric glow due to neutral interstellar helium and neutral interstellar hydrogen performed from the Nozomi spacecraft in a transition orbit from Earth to Mars are discussed in search for a possible deflection of the upwind direction of hydrogen with respect to helium. Although a deflection of the secondary component of interstellar hydrogen could not be entirely ruled out in this study, the observations confirm the baseline direction of the inflow. Observations suggest that the helium flow arrives from the ecliptic coordinates of (258.7 ± 3.4°), which within error bars is consistent with the primary helium flow direction derived from direct observations (e.g. Witte et al. 2004), and that the longitude of the hydrogen flow is equal to 255.416 ± 5°, which is consistent with both the canonical helium direction and the direction suggested for hydrogen by Lallement et al. (2005). One- and two-component simulations of interstellar neutral hydrogen and one-component simulations of interstellar helium were performed in an attempt to explain the features of the observed emission distribution in the inner heliosphere. Comparison of Nozomi UV measurements with simulations suggests that adding a secondary flow component to a one-component LIC-flow model brings a better agreement with observations, but is not able to explain all details of the results. Although the present simulations provided some insights into the processes operating within the heliospheric interface, further investigation of interaction of the solar wind with local interstellar gas, and of the parameters characterizing the global heliospheric structure are fully warranted.

Acknowledgements. H. Nakagawa was supported by the Scientific Research Fund of the Japan Society for the Promotion of Science (JSPS). The authors wish to thank Dr. R. Lallement for providing the classical model code, Dr. E. Quémerais and Dr. V. Izmodenov for valuable discussions, and the ISSI Interstellar Hydrogen team for attentive feedback. Especially, we thank Dr. E. Möbius for his valuable comments. This research profited from the database of the OMNI WEB and from the SOLAR2000 model due to SpaceWx. M. Bzowski was supported by Polish Ministry of Scientific Research and Information Technology Grants 1P03D 009 27 and N522 002 31/0902.

References

Baranov, V. B. 2006, ISSI Sci. Rep., SR-005, 1
Baranov, V. B., & Malama, Y. G. 1993, J. Geophys. Res., 98, 15157
Baranov, V. B., & Malama, Y. G. 1995, A&A, 304, 14755
Barnett, C. F., Hunter, H. T., Kirkpatrick, M. I., et al. 1990, Tech. Rep. ORNL-6086, 1, Oak Ridge National Laboratory, Oak Ridge, TN
Bertaux, J. L., & Lallement, R. 1984, A&A, 140, 230
Bertaux, J. L., Kyrölä, E., Quémerais, E., et al. 1995, Solar Physics, 162, 403
Bertaux, J. L., Quémerais, E., Lallement, R., et al. 2000, Geophys. Res. Lett., 27, 1331
Bzowski, M. 2001, Space Sci. Rev., 97, 379
Bzowski, M. 2001, COSPAR Colloquia Series, 11, The Outer Heliosphere: The Next Frontiers (Pergamon: Elsevier), 69
Bzowski, M., Möbius, E., Tarnopolski, S., et al. 2008, A&A, 491, 7
Bzowski, M., Mäkinen, T., Kyrölä, E., Summanen, T., & Quèmerais, E. 2003, A&A, 408, 1165
Collier, M. R., Moore, T. E., Simpson, D., et al. 2004, Adv. Space Res., 34, 166
Costa, J., Lallement, R., Quémerais, E., et al. 1999, A&A, 349, 660
Cruddace, R. F., Paresce, S., Bowyer, S., & Lampton, M. 1974, ApJ, 187, 497
Decker, R. B., Krimigis, S. M., Roelof, E. C., et al. 2005, Science, 309, 2005

Fahr, H. J. 1978, A&A, 66, 103

Fukunishi, H., Watanabe, S., Taguchi, M., & Takahashi, Y. 1999, Adv. Space Res., 23, 1903

Gloeckler, G. 1996, Space Sci. Rev., 78, 335

Gloeckler, G., Möbius, E., Geiss, J., et al. 2004, A&A, 426, 845

Izmodenov, V. 2001, Space Sci. Rev., 97, 385

Izmodenov, V., & Baranov, V. B. 2006, ISSI Sci. Rep., SR-005, 67

Izmodenov, V., Malama, Y. G., Gloeckler, G., & Geiss, J. 2003, ApJ, 594, L59

Izmodenov, V., Malma, Y., Gloeckler, G., & Geiss, J. 2004, A&A, 414, L29

Izmodenov, V., Alexashov, S., & Myasnikov, A. 2006, A&A, 437, L35

Izmodenov, V., Malama, Y. G., Runderman, & Michael, S. 2008, Adv. Space Res., 41, 318

Lallement, R., Bertaux, J. L., & Dalaudier, F. 1985, A&A, 150, 21

Lallement, R., Quémerais, E., Bertaux, J. L., et al. 2005, Science, 307, 1447

Lemaire, P. L., Emerich, C., Vial, J. C., et al. 2002, ESA SP-508, 219

Möbius, E., Bzowski, M., Chalov, S., et al. 2004, A&A, 426, 897

Nakagawa, H., Fukunishi, H., Watanabe, S., et al. 2003, J. Geophys., Res., 108, 8035

Nakamura, M. K., Yamashitak, Yoshikawa, I., et al. 1999, Earth, Planets and Space, 51, 61

Okazaki, Y., Fukunishi, H., Takahashi, Y., Taguchi, M., & Watanabe, S. 2005, J. Geophys., Res., 110, A03104

Quémerais, E. 2000, A&A, 480, 353

Quémerais, E., & Bertaux, J. L. 2002, Geophys. Res. Lett., 29, 1018

Quémerais, E., & Izmodenov, I. 2002, A&A, 396, 269

Quémerais, E., Bertaux, J. L., Lallement, R., et al. 1999, J. Geophys. Res., 104, 12585

Ruciński, D., & Bzowski, M. 1995, Adv. Space Res., 16, 121

Sitarski 1979, Acta Astron., 29, 401

Stone, E. C., Cummings, A. C., McDonald, F. B., et al. 2005, Science, 309, 2017

Taguchi, M., Fukunishi, H., Watanabe, S., et al. 2000, Earth, Planets and Space, 52, 49

Thomas, G. E. 1978, A&A, 6, 173

Tobiska, W. K., Woods, T., Eparvier, F., et al. 2000, J. Atm. Terr. Phys., 62, 1233

Vallerga, J., Lallement, R., Lemoine, M., et al. 2004, A&A, 426, 855

Witte, M. 2004, A&A, 426, 835

Wu, F. M., & Judge, D. L. 1979, ApJ, 231, 594

Yamazaki, A., Yoshikawa, I., Shiomi, K., et al. 2006, J. Geophys., Res., 111, A06106

Yoshikawa, I., Yamazaki, A., Shiomi, K., et al. 2000, J. Geophys., Res., 106, 26057

Yoshikawa, I., Yamazaki, A., Shiomi, K., et al. 2001, J. Geophys., Res., 106, 25745

Zank, G. P. 1999, Space Sci. Rev., 89, 413

Zank, G. P., Pauls, H. L., Williams, L. L., & Hall, D. T. 1996, J. Geophys. Res., 101, 21636